0.1 The Solar-Terrestrial Environment

The solar terrestrial environment begins with the Sun in the center of the solar system. The Sun, like most stars, is composed of highly energized plasma that is gravitationally bound together. This makes it an extremely complex and highly dynamic system that is constantly interacting with the rest of the solar system. The surface of the Sun is populated with sunspots, dark, relatively cool regions with intense magnetic fields, as well as coronal holes, which are low density areas characterized with a continuous outflow of plasma. The intense magnetic fields associated with sunspots can break down releasing a large amount of energy and plasma, known as a solar flare. Planet-sized globs of plasma known as coronal mass ejections (CMEs) can be ejected from the surface, which can be large enough to maintain an internal magnetic field as they travel through the solar system. The frequency of sunspots and large outbursts of plasma changes with the 22-year long solar cycle. A large number of Sun spots, high occurrence of fast, dense plasma outbursts, and a highly variably magnetic field indicate solar maximum. Conversely, solar minimum is characterized by a low Sun spot number and slow and relatively steady outflow

The Sun interacts with the rest of the solar system through the solar wind, a continuous outflow of plasma that caries the Sun's magnetic field with it. The solar wind typically has a density around 10 cm^{-3} at Earth and is traveling away from the Sun at approximately 400 km/s. However, like the Sun, the solar wind is highly dynamic and these parameters can change drastically over a period of minutes. CMEs, for instance, create a substantial increase in density and are often proceeded by a shock. In addition to the outflow of plasma, the solar wind also consisted of the Sun's magnetic field extended into the outer limits of the solar system, called the interplanetary magnetic field (IMF). Because the Sun has a short rotation period (about 33 days), the IMF gets twisted into a spiral, commonly called the Parker Spiral [Parker, 1958]. When the IMF reaches the Earth, the magnetic field is typically oriented at a 45° inclination relative to the ecliptic, but this is highly variable depending on solar wind conditions.

The IMF interacts with the Earth's own magnetic field, the magnetosphere. Without outside influences, the magnetosphere would be approximately a dipole field, but dynamic pressure from the solar wind causes the Sun facing side to be compressed to 6–10 Earth radii and the rear side to be stretched into an extended tail (hundreds of Earth radii). Because the solar wind is typically a supersonic flow, a bow shock forms on the dayside of the magnetosphere. The heated and compressed solar wind plasma created by the bow

shock is known as the magnetosheath. The magnetopause is the actual boundary between solar wind plasma in the magnetosheath and magnetospheric plasma. However, the magnetosphere is not fully closed. At the magnetopause, magnetic reconnection can occur between the IMF and the Earth's magnetic field creating open field lines. Magnetic field lines originating from the Earth are then directly connected to the Sun through the solar wind, which consequently allows highly energized solar particles to enter the magnetosphere. Open field lines tend to occur around the Earth's polar caps, making these regions particularly interesting to study due to very complex behavior and coupled interactions between the Earth and the Sun.

Closer to the Earth's surface, the magnetosphere also interacts with the Earth's ionosphere, a layer of partially ionized plasma in the upper atmosphere. The interaction between charged particles in the ionosphere with magnetic field lines from the magnetosphere couples these two regions and creates non-trivial dynamics. In addition, highly energized charged particles from the solar wind travel along open field lines and collide with both ions and neutral particles in the ionosphere, creating the aurora at high latitudes. Below the ionosphere, the thermosphere consists mostly of neutral particles, however neutral winds can influence the ionosphere through viscous interactions along the lower boundary. Overall, the charged particle interactions in the ionosphere create a highly complex system, which is further complicated by coupling with both the thermosphere from below and the magnetosphere and solar wind from above.

0.2 The Earth's Ionosphere

The Earth's ionosphere is a region of the upper atmosphere that ranges approximately between 50–1000 km in altitude where neutral gases have been excited so that they are partially ionized, resulting in free electrons and ions mixed with neutral particles. Two conflicting processes occur in the ionosphere to create a peak in electron density, commonly referred to as the Chapman Layer **CTIE CHAPMAN?**. Solar illumination and particle precipitation ionize neutrals, and the density of ions increase as altitude decreases because there are more neturals available to ionize. However, below a certain point, the concentration of ions becomes large enough that recombination into neutral particles becomes a substantial factor, reducing the ion density. The exact altitude where this density peak occurs is variable with time of day, location, season, and solar cycle. A profile of how electron density changes with altitude is shown in Figure 0.1, found from the International Refer-
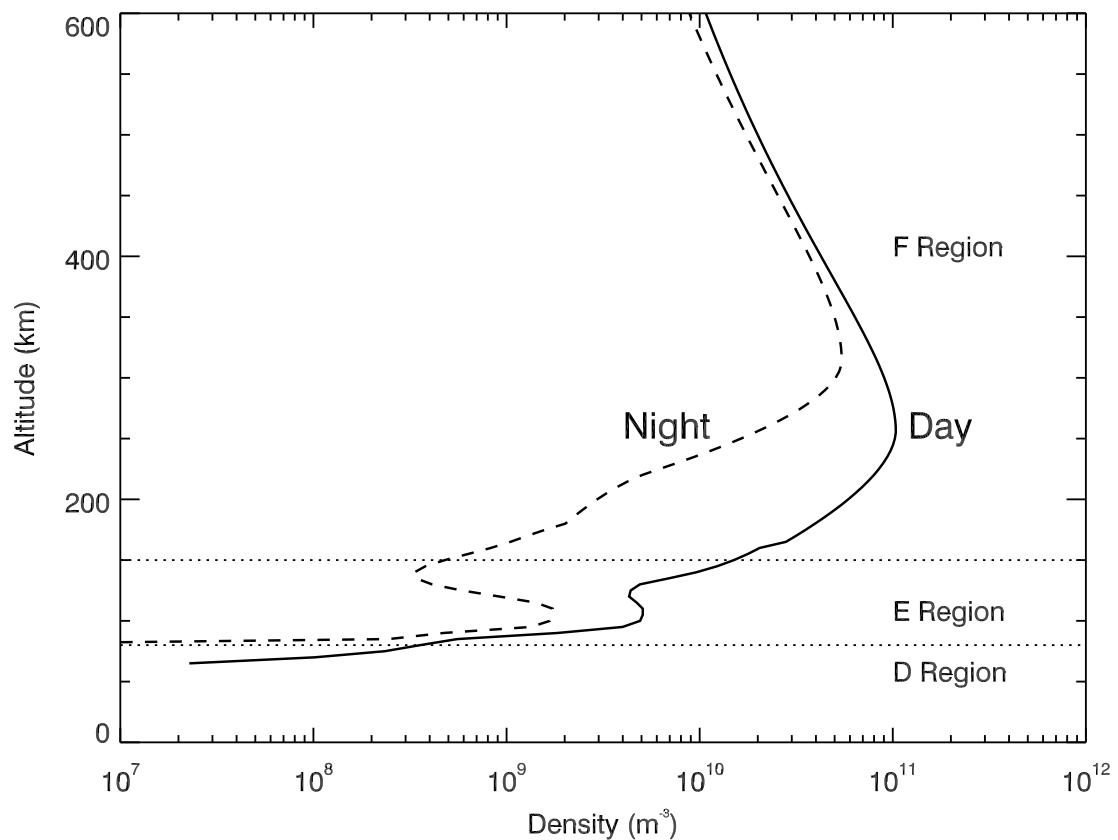
Figure 0.1. Altitude profile of electron density throughout the ionosphere found from the IRI model. Typical ranges of the D, E, and F regions are identified.

ence Ionosphere (IRI) model run on January 1, 2007 at 75° N, 0° E, geographic (discussed further in Section 0.3.3).

Above 50 km, the primary neutral particles are atomic oxygen, O, molecular oxygen, O_2, and molecular nitrogen, N_2. Common ions at these altitudes are therefor mostly composed of oxygen and nitrogen, O^+, NO^+, O_2^+, N_2^+, but hydrogen, H^+, can contribute as well [Kelley, 2009]. In the ionosphere, neutral densties are typically several orders of magnitude higher than ion densities, however even a small number of charged particles changes the behavior of the region dramatically. Because there are so many different ion species, plasma density is usually discussed simply in terms of electron density

4

0.2.1 Ionosphere Regions

The ionosphere is typically divided into three region, Figure 0.1. The D region is located between 80 and 90 km in altitude and typically only exists in the daytime when the ionosphere is sunlit. The E region typically exists between 90 and 120 km with a density peak between 105 and 110 km, depending on factors such as time of day and season. Above 120 km is considered the F region, which has a density peak between 300 and 400 km. The F region can actually have two peaks under some daytime conditions, notated as the F1 peak and the F2 peak. The locations and peak densities of each of these regions is highly variable both diurnally and seasonally. In Figure 0.1, the daytime profile is shown with the solid line next to a nighttime profile with a dashed line. Note that night electron densities are lower at all altitudes due to the lack of photoionization durring nighttimes. In addition, the F-region peak moves to higher altitudes at night.

Because the concentrations of ions and neutral particles changes with altitude, each of these regions have distinct plasma physical properties that make them unique and change how plasma structuring forms. The main change that occurs is wether the the large-scale motion of a particle is controlled more by the magnetic field (the particle is magnetized) or by collisions with other particles (collisional). This can be determined by comparing the collision frequency, ν_α, to the gyrofrequency, Ω_α, of a particular species. If $\Omega_\alpha \gg \nu_\alpha$, the particle completes many gyrations between each collision, so its motion is determined mostly by the magnetic field and it is magnetized. If $\nu_\alpha \gg \Omega_\alpha$, the particle collides with other particles much more often than it complete a gyration, so it is considered collisional. The gyrofrquency is dependent on the mass and charge of the particle and the strength of the magnetic field, $\Omega_\alpha = q_\alpha B / m_\alpha$, so is roughly constant through the ionosphere because the magnetic field strength does not change much through these altitudes. The collision frequency depends on the density of a species relative to the density of all other species in the plasma and can be calculated from a series of complicated expressions [Schunk and Nagy, 1980, 2009]. In the E region, $\Omega_e \gg \nu_e$, so electrons are magnetized. However, the motion on ions is dominated by collisions between ions and neutrals ($\nu_i > \Omega_i$), so ions in the E region are considered collisional. In the F region where the neutral density is much lower, both ions and electrons are magnetized, $\Omega_\alpha \gg \nu_\alpha$. These differences in how charged particles move vary the conductivity and can strongly impact how plasma waves develop, which will be discussed further in Section ??.

0.2.2 Plasma Structuring in the Polar Ionosphere

The polar ionosphere is a particularly interesting and dynamic region due to the presence of the magnetic poles and open field lines to the solar wind. Plasma structuring can occur as variations in density, velocity, or temperature, but the main focus of this work will be density perturbations, often called irregularities. Density irregularities in the polar cap can occur on scales ranging from thousands of kilometers to less than a centimeter [Tsunoda, 1988]. Large-scale plasma irregularities are typically considered to be any density structuring on the scale of $1 - 1000$ km. Some common examples are polar patches, polar holes, and sun-aligned arcs. Polar patches are large density enhancements (usually at least twice the background plasma density) that travel across the polar cap with the background convection. Polar holes are plasma density depletions that typically occur in the F region slightly poleward of the auroral oval. Sun-aligned arcs are large density forms that stretch across the polar cap along the sun-earth line. They are very narrow and often characterized by large and complex velocity shears on either side of the arc.

Intermediate-scale structuring typically ranges from 100 m $- 1$ km. This is also referred to as scintillation-causing structuring and is responsible for many of the negative space weather effects that are observed on Earth. Radio signal scintillation through the ionosphere changes the phase and amplitude of the original signal, which can effect the ability that satelites have to communicate with ground recievers. This can cause communication blackouts or introduce large errors into GPS calculations, effecting navigation. Because communication and navigation technology is implemented in both every day civilian life as well as government and military intrests, the effects of this kind of signal scintillation can be far reaching.

Small-scale structuring is generally considered to be all irregularities less than 100 m. Although the effects of these scale sizes on navigation and communication systems are minimal, they can be the easiest to study because of large data sets collected from high frequency ionospheric radars globally for several decades (discussed further in Section 0.3.1). The irregularity sizes presented here are rough categories only and a high degree of coupling between different scales is generally considered reasonable. For instance, large-scale structures such as polar patches may very well have internal intermediate- or small-scale structuring. Some kind of turbulent cascade is often assumed to connect these different scales, but because various instruments or techniques usually only observe structuring on

a particular scale, it is difficult to find direct evidence of this or how exactly it occurs.

0.3 Observational Techniques and Models

0.3.1 Coherent Scatter Radars

Coherent Scatter Radars (CSR) have been used to study the ionosphere for the last half century. The radar transmits a radio wave, which can reflect off plasma structuring in the ionosphere, and then be detected by the recieving antennas. The time difference between when the signal was transmitted and when it was detected and the power and phase of the returned signal can then be used to determine local characteristics of plasma irregularities.

There are three measurements typically made by CSR systems: backscatter power, line of sight (LoS) velocity, and spectral width. Backscatter power is the power of the retuned signal that the radar's recievers detect. Typically, a threshold is selected for the minimum power acceptable for a return to be considered an actual signal instead of background noise. LoS velocity is the component of the total plasma drift velocity that is measured along one beam of a radar. Because radars measure velocity through the doppler shift of backscatter, only the component of the velocity vector that is along the radar beam can be measured. Spectral width represents the width of the doppler power spectrum and can determine some of the characteristics of irregularities [Greenwald et al., 1985].

CSR systems typically operate by transmitting pulses instead of continuously. This allows the distance between the radar and the target to be found (based on the time difference between when the pulse is transmitted and received). The size of the range gate is determined by the length of a radar pulse, Equation 0.1.

$$\Delta r = \frac{c\Delta t}{2}$$ (0.1)

Longer pulses result in larger range gates, resulting in poorer spatial resolution.

When the radar transmits continuously, backscatter will be received, but because it is impossible to know when that signal was transmitted, the difference in time between transmission and receiving cannot be used to calculate how far away the backscatter volume is. Conversly, if the radar only transmits a pulse of a certain length of a certain length and then "listens" for its return, the time between transmission and return is known and the distance the pulse traveled can be calculated and therefore the location of the backscattering volume. However, using this simple single-pulse method another pulse cannot be transmitted until the first pulse returns, limiting the temporal resolution that can be

achieved. This can be improved by using a multipulse scheme, which will be discussed below.

A short time between pulse returns is nessisary to allow dopler velocities to be calculated, particularly at long ranges. The maximum dopler shifted frequency that can be observed by a radar is the Nyquist frequency, which is equivilent to half the sampling frequency, Equation 0.2.

$$f_n = \frac{f_s}{2} \tag{0.2}$$

Radars operating in single-pulse mode have a very limited sampiling frequency, as described above, particularly at long ranges where the pulse must travel a long distance. This severely limits the dopler shift that can be measured, which places an upper limit on the LoS dopler velocity that can be calculated with this technique. For an ionospheric radar observing a structure 2000 km away, it would take about 13 ms for a signal traveling at the speed of light to travel to the the structure and back to the radar, wich corresponds to a sampling frequency of $f_s = 75$ Hz. The Nyquist frequency is then $f_n = 37.5$ Hz, which corresponds to a maximum measurable Doppler velocity of ~ 550 m/s. Flows in the ionosphere have been known to exceed 1000–2000 m/s, so single pulse sampling is insufficient for these purposes.

Instead of waiting for each individual signal to be recieved before transmitting the next, ionospheric radars typically employ a multipulse mode. In a multipulse mode, the radar transmits a series of pules with different time intervals or lags between them. This can introduce complications when backscatter from different pulses at different ranges is received by the radar at the same time, referred to as cross-range interference, but these effects can be mitigated using correlation techniques. The smallest lag between two pulses is known as the multi-pulse increment, τ. All other lags are integer multiples of τ, which allows the calculation of the corresponding lags of the complex autocorrelation function (ACF). The ACF is used to find the spectral characteristics of the backscatter, from which the LoS velocity, spectral width, and backscatter power can be obtained. Overall, multipulse techniques are generally considered far more appropriate for ionospheric studies than single pulse [Farley, 1972, Greenwald et al., 1983, 1985, Barthes et al., 1998, Ponomarenko and Waters, 2006].

The first instance of CSR being used to study plasma density structures in the ionosphere was the Scandanavian Twin Auroral Radar Experiment (STARE) in the 1970s and 1980s. STARE consisted of two very high frequency (VHF) radars with overlapping FoVs

that were designed to measure FAIs in the E region of the ionosphere [Greenwald, 1997]. The advantage of two radars with overlaping FoVs was the ability to observe the same structures from two different orientations, Because each radar can only measure the LoS velocity of a structure, two simultanious observations from different directions allows two different velocity vecotor compontents to be found, and hense the total velocity vector can be calculated. This technique is still commonly used with CSR system.

Super Dual Auroral Radar Network (SuperDARN)

The Super Dual Auroral Radar Network (SuperDARN) is a global network of HF CSRs that was designed to measure small-scale plasma structuring in the ionosphere and map the global plasma convection. The network currently consists of about 35 operational radars between the northern and southern hemispheres distributed at mid-, high-, and polar latitudes, Figure 0.2. Following the STARE experiment [Greenwald et al., 1978], the first HF ionospheric radar was built in Goose Bay, Canada in 1983, which would become the first of the SuperDARN radars [Greenwald et al., 1985].

It is nessisary to use HF radars to study ionsospheric structures in the polar cap because the magnetic field is close to vertical and in order for the radar beam to meet the perpendicularity condition to observe FAIs, the beam must be refracted through a dense ionosphere. VHF radar beams are not refracted enough in the polar cap and the beam will pass through the ionosphere without reflecting off any FAIs. SuperDARN radars operate at a nominal 8–20 MHz frequency, which, according to the Bragg scatter equation for backscatter, corresponds to observing decameter-scale plasma waves. Each radar consists of 16 independent transmit and recieving antennas. Beams are electronically steerable and most radars have between 16 and 24 beams in normal operation mode, each beam being $3.25°$ in azimuth. Each beam consists of 75–100 range gates, which are generally either 15 km or 45 km in length [Chisham et al., 2007]. SuperDARN radars were originally designed to used a 7 pulse ACF [Farley, 1972, Greenwald et al., 1983, 1985], however since 2011, most radars have begun using an 8 pulse sequence. The multi-pulse increment, τ, is 2400 μs, which corresponds to a Nyquist frequency of about 200 Hz, small enough to measure plasma drift velocities up to 3000 m/s. The spectral characteristics of backscatter of recovered from the ACF using the FITACF algorithm [Ponomarenko and Waters, 2006].

One of the original purposes of SuperDARN was to produce maps of the plasma convection patterns in the polar caps using 2D velocity vectors. Originally this was accom-
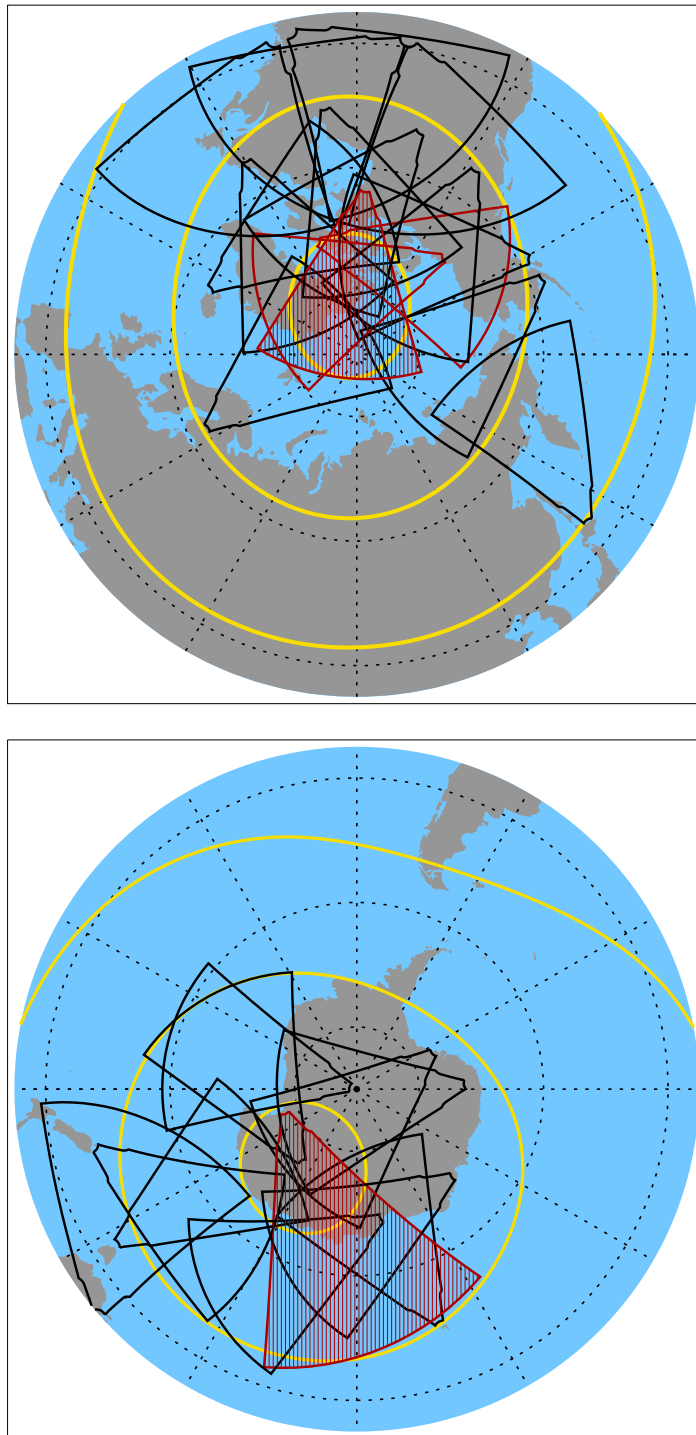
Figure 0.2. FoVs of all operational SuperDARN radars in both the northern (left) and southern (right) hemispheres. Polar latitude radars are shown with the red outlines. The radars at Rankin Inlet (northern hemisphere) and McMurdo Station (southern hemisphere) are shaded in red because these two instruments are particularly important in the following studies. Lines of constant magnetic latitude are shown in yellow at $\Lambda = 40°, 60°, 80°$ in the northern hemisphere and at $\Lambda = -40°, -60°, -80°$ in the southern hemisphere.

plished by considering two radars with overlapping FoVs. If both recieved backscatter from the same scattering volume, two LoS velocities could be found for that scattering volume, which could be combined to find a 2D velocity vector [Ruohoniemi et al., 1989]. The modern method for creating convection maps involves taking all data recorded by all radars in a particular hemisphere and finding the best fit to a 2D ionospheric electrostatic potential using Legendre functions [Ruohoniemi and Baker, 1998]. For convection maps, only data from the F region is considered. If there is not enough velocity data to confine the fit sufficiently, the measured data points are supplimented with a statistical model based on solar wind IMF conditions [Ruohoniemi and Baker, 1998]

Because convection maps require data covering as wide a range of magnetic local time sectors as possible, SuperDARN radars are continuously operational, usually in a common mode. This creates a vast database of high-quality measurements of small-scale FAIs, which is very useful for other studies on irregularity occurrence and plasma structuring. In the studies presented here, data was primarily used from the SuperDARN radars located at Rankin Inlet, Canada (RKN) and McMurdo Station, Antarctica (MCM). The have been shaded in Figure 0.2.

0.3.2   Incoherent Scatter Radar

Similar to CSRs, incoherent scatter radars (ISRs) are ground based radars that are used to probe the ionosphere. However, they use a fundamentally different technique to observe structuring, which allows them to measure parameters of the actual ionospheric plasma. Where as CSRs receive backscatter from relatively large, "coherent" density structures in the ionosphere, ISRs operate by radar beams scattering due to the random thermal motion of electrons in the plasma. The radar receivers then detect a spectra of frequencies with different power [Gordon, 1958].

The scattering cross section for a volume of N electrons in the ionosphere is given by $\sigma_n = N\sigma_e$ for radio waves with a wavelength small compared to the Debye length of the plasma, where σ_e is the scattering cross section of a single electron [Gordon, 1958, Fejer, 1960]. The relationship to the plasma Debye length is important because at scale sizes smaller than the Debye length, the plasma is not capable of organized motion, so the motion of the elections is only due to their own thermal energy and not larger scale plasma waves. The signal returned from this kind of scatter was postulated to have a very low power and a very broad spectral width, however after the first ISR was built,

the spectrum was found to be much narrower than previously expected [Evans, 1969]. This can be attributed to the effect that the much slower ions have on free electrons in the plasma through ion acoustic waves [Bowles, 1958]. The practical results of this is that ISRs can use radio waves of a much longer wavelength than originally anticipated, on the order of ~1 m.

Analysis of the returned power spectrum reveals the electron density, electron and ion temperatures, and LoS ion velocity [Evans, 1969, Rishbeth and Williams, 1985, Nicolls et al., 2007]. Using a model of chemical composition at different altitudes, the average ion mass can also be found. In addition, 3D convection velocities and electric field vectors can be derived from LoS ion velocity measurements in some of the more modern ISRs by assuming both $\mathbf{E}$ and $\mathbf{V}_E$ are constant across the radar's FoV [Heinselman and Nicolls, 2008]. Each instrument must be calibrated with known electron density measurements to account for noise and system constants [Nicolls et al., 2007]. This is done using the plasma frequency measured from either the plasma line of the ISR spectra during summer daytime period or ionosonde measurements for all other times [Bahcivan et al., 2010, Themens et al., 2014].

The first ISR was built in Arecibo, Puerto Rico in the 1950s [Gordon, 1958]. Since then, at least 8 other ISRs have been deployed around the world at equitoral, mid-, and high-latitudes. The most recent advancement has been the development of Advanced Modular Incoherent Scatter Radars (AMISR), of which there are currently three in use, one at the Poker Flat Rocket Range, just north of Fairbanks, AK and two in Resolute Bay, Canada. The advantage of these new systems is that they are electronical steerable, unlike older ISRs which consisted of a large dish that had to be moved manually to change the beam direction. This allows beams to be transmitted in many different directions at a very high time cadence, giving the radar the capability to make measurements in multiple directions almost simultaneously [Nicolls et al., 2007, Nicolls and Heinselman, 2007, Bahcivan et al., 2010]. This is very important for creating 2D maps of ionospheric conditions and tracking how they change in time [Semeter et al., 2009, Dahlgren et al., 2012b,a]. AMISR systems typically have two types of pulses, a long pulse (LP) with 72 km range gates for F-region studies and an alternating code pulse (AC) with 4.5 km range gates gates for E region studies. The exact number and configuration of beams depends on the radar mode used and can be changed easily due to the system's electronic steering. In the common WorldDay mode, there are typically 11 beams and data is collected at ~1 min intervals, although this

can change slightly between different renditions of the WorldDay mode.

One of the most important advantages of ISR systems over CSRs is the ability to directly measure electron density in the ionosphere. However, because ISRs are much scarcer and are only typically run on in WorldDay mode a few days out of every month, data is not as widely available. In addition, ISRs do not actually measure small-scale coherent plasma structures like the HF SuperDARN network does. However, they can directly measure large-scale structures and image density variations on scales larger that 100 km (limited by the number of beams and range gate size). For these region, it is often useful use a combination of CSR and ISR measurements in ionospheric plasma structuring studies, when possible. The primary ISR used in the following studies is the north face of the AMISR system at Resolute Bay, Canada, RISR-N. The FoV of RISR-N overlaps that of the RKN SuperDARN radar, making it ideal for these types of comparison studies.

0.3.3 IRI Model

The International Reference Ionosphere (IRI) is an empirical model of the Earth's ionosphere. It was originally created in 1969 as a joint effort between the Committee on Space Research (COSPAR) and the International Union of Radio Science (URSI) and has been periodically updated since then [Rawer et al., 1975, 1978, 1981, Bilitza, 1985, 1986, Bilitza and Rawer, 1990, Bilitza, 1997, 2001, Bilitza and Reinisch, 2008]. The current version is IRI-2012 [Bilitza et al., 2014], which is used throughout the work done here. It can be accessed either as an online module or by downloading and running the FORTRAN source code, both of which are available from the International Reference Ionosphere website (http://iri.gsfc.nasa.gov/).

The IRI model can produce outputs of electron density, temperatures of electrons, ions, and neutrals, ion composition (O+, H+, He+, O2+, NO+, N+), and total electron content (TEC). The model requires the input of a location (latitude, longitude, and altitude) and time (year, date, and time). Additionally, the model gives the option to choose between two F peak models and three bottomside thickness models. There are a variety of other optional input parameters such as sunspot number, ionospheric index, and F10.7 radio flux which can help make the output parameters more accurate for a particular situation. Internally, the model has the additional capability of producing profiles of any of the output parameters in either space or time. This is particularly significant for height profiles, and allows the peak heights and densities of the E and F region to be calculated.

Although the IRI model is very useful for providing background plasma density conditions where no instruments are available to make real measurements, it is important to remember that it is a model and therefor only represents the average conditions. Although it is fairly accurate at mid-latitudes [Coïsson et al., 2006, Bilitza et al., 2012], it does not necessarily represent variations within the polar cap well [Themens et al., 2014, Makarevich et al., 2015]. In particular, the height of the F-region peak tends to be underestimated in daytime and the bottomside thickness does not show realistic seasonal and diurnal variation [Themens et al., 2014]. Despite this, the IRI model is still a very important tool for establishing a density profile at any time in any location in the ionosphere. And example of an altitude profile of plasma density provided by the IRI model is shown in Figure 0.1. The displayed profiles shows how the electron density changes with altitude at local noon (day) and midnight (night) on January 1, 2007 at 75° N, 0° E, geographic.

One of the most important uses of the IRI model has been its integration into ray tracing simulations. It can be valuable to determine the degree to which HF radar beams refract through a dense ionosphere. This can be done through standard raytracing tools based on numerical solutions to the Hamiltonian raypath equations [Haselgrove, 1963, Jones and Stephenson, 1975], however these tools require a 2D density profile along the path that the radar beam travels. It is possible to assume a Gaussian distribution or Chapman layer as a simple model of the F-region peak, but it is much more instructive to use output from the IRI model, as it is sensitive to changes in latitude as well as seasonal and diurnal variations.

0.4 A Brief Review of Plasma Structuring Theory and Observations in the Polar Cap

Much work has been done over the past several decades to study the complicated picture of plasma structuring in the polar cap, including theoretical analysis of plasma dispersion relations, simulations of plasma dynamics, and observations of plasma structuring using a variety of instruments. Here, a survey will be given of some of these advancements and the current state of understanding plasma structring on a range of scales.

0.4.1 Theory and Simulations of Polar Patches and Plasma Instabilities

Large-scale structuring in the polar cap can take a variety of forms, Section 0.2.2, but here we will focus on large regions of enhanced plasma density known as polar patches [Weber et al., 1984, 1986, Buchau et al., 1983, 1985, e.g.]. The first observations of polar patches were made in the 1960s by Hill [1963]. They can range in size up to 1500 km in diameter

and can have peak densities as much as eight times that of the background ionospheric plasma [Weber et al., 1986, Hosokawa et al., 2014]. Polar patches are know to emerge on the dayside and then propagate with the background plasma convection across the polar cap to the nightside, where they either disintegrate or recombine with enhanced-density plasma in the auroral oval [Weber et al., 1985, 1986].

There have been at least 6 mechanisms proposed for how polar patches form on the dayside [Crowley, 1996, Carlson, 2012].

1. Discrete changes in solar wind parameters, usch as IMF, density, speed, and pressure [Sojka et al., 1994]

2. Average flow patterns varying in time [Anderson et al., 1988]

3. Transient magnetopause reconnection [Lockwood and Carlson, 1992]

4. Plasma production by cusp particle precipitation [Rodger et al., 1994, Millward et al., 1999]

5. Plasma flow jet channels that cut continuous streaches of plasma into segments [Valladares et al., 1998]

6. Alfven wave coupling [Prikryl et al., 1999]

Although particle precipitation has been shown to create enhanced plasma density in the cusp region [Rodger et al., 1994], it is unreasonable for this mechanism to account for the largest density enhancements observed in polar patches. These high densities must originate from the resivor of solar illuminated plasma on the dayside. Additionally, a mechanism is still required to separate patches from the cusp region. High speed flow channels can "cut" segments off of a tongue of high-density plasma that has been pulled into the polar cap by convection [Valladares et al., 1994, 1998]. Models have also shown changing large scale convection patterns quickly in time does produce density structures similar to patches [Anderson et al., 1988]. However, the mechanism that seems to be dominant for the majority of polar patches observed is transient magnetic reconnection [Carlson, 2012].

In order to discuss patch formation by transient magnetic reconnection, it is important to first understand the steady-state ionospheric convection patterns in the polar cap and how they relate to the magnetosphere [Cowley, 1980]. Figure 0.3 is a schematic of how the IMF, magnetosphere, and ionospheric polar cap are all interconnected. In general,

magnetic field lines in the magnetosphere can either be closed (grey lines in Figure 0.3), meaning they connect only the north and south pole of the earth, or open (light blue lines in Figure 0.3), when one of the ends of the field lines originates from the sun such that the field line is connected directly to the IMF. IMF lines that are not connected to the earth are shown in dark blue in figure 0.3. The polar cap boundary is generally defined as the border between open and closed magnetic field lines, shown by the green line in Figure 0.3.

By Faraday's Law, the total electromotive force, ξ around the polar cap boundary is equal to the rate of change of magnetic flux, Φ_B within the polar cap, Equation 0.3 [Lockwood and Cowley, 1992]. In steady-state solutions, $d\Phi_B/dt = 0$, so $\xi = 0$ by definition, however the polar cap is known to be a highly dynamic system, so changes in magnetic flux are expected.

$$-\xi = \frac{d\Phi_B}{dt} = B\frac{dA_{pc}}{dt} \tag{0.3}$$

In the polar cap at ionospheric altitudes, the magnetic field strength is relatively constant at around 5×10^{-5} T, so any changes in magnetic flux must be due to changes in the polar cap area, A_{pc} due to the polar cap boundary expanding or contracting [Lockwood and Cowley, 1992]. The polar cap boundary changes in response to magnetic reconnection between the magnetosphere and the IMF on both the day and night sides changing the amount of open magnetic flux.

Magnetic reconnection between the IMF and the Earth's magnetosphere occurs along the X-line on the dayside magnetopause (red line in figure 0.3). The X-line in the magnetopuase can be mapped along the magnetic field lines (orange) to the ionosphere, where it is referred to as the merging gap (pink dotted line in figure 0.3) and lies along the steady state polar cap boundary.

During reconnection events, the polar cap boundary moves equatorward as the open magnetic flux into the polar cap increases, Figure 0.3 [Cowley et al., 1991, Lockwood and Cowley, 1992]. In addition, the potential along the X-line also gets mapped to the merging gap, assuming there is minimal drop in potential along the magnetic field lines [Lockwood and Carlson, 1992]. The combination of these two effects results in flux being transferred across the boundary at a rate equal to the applied voltage along the X-line and hence plasma flow across the merging gap [Lockwood and Carlson, 1992], as seen in Figure 0.4.

Figure 0.4 is a schematic of how transient magnetopause reconnection forms polar patches. In all panels, the the dayside is the top of the figure and the green line shows the
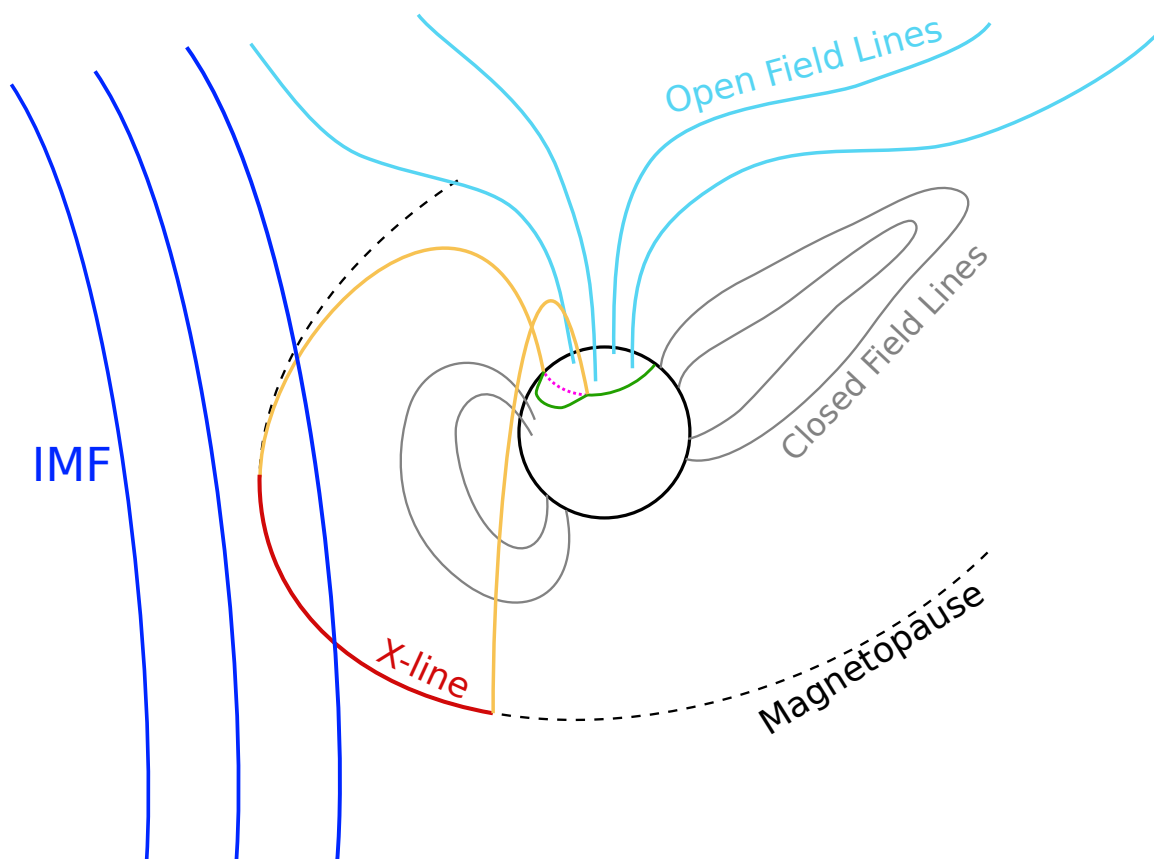
Figure 0.3. Diagram of the interactions between the IMF, magnetosphere, and polar cap ionosphere. Closed field lines in the Earth's magnetosphere are shown in grey while open field lines are light blue. The polar cap open-closed boundary is in green. Magnetic field lines that are part of the IMF are shown in dark blue. Magnetic reconnection occurs along the X-line (red) on the dayside of the magnetopause (dashed line). The X-line can be mapped back along magnetic field lines (orange) to the ionosphere, where their projection is the merging gap (pink dotted line). Durring reconnection events, the open-closed boundary expands equatorwards as more open field lines are formed and there is plasma flow across the merging gap.

open-closed polar cap boundary, similar to Figure 0.3. Plasma flow contours are shown in black and the ~~light~~ orange region represents high density from the dayside reservoir. The reconnection burst starts ~~at~~ Figure 0.4a and the increasing amount of open magnetic flux moves the dayside open-closed boundary equatorwards, as described above [Cowley et al., 1991].

As reconnection continues in Figure 0.4b, the open-closed boundary continues to expand equatorwards as more open flux is produced, which excites a convection pattern in the polar cap [Cowley et al., 1991]. Simultaneously, this convection starts to transport dense dayside plasma polewards [Lockwood and Carlson, 1992]. As more open flux is produced, Figure 0.4c, the strength of the plasma flow increases and a large blob of dense, dayside plasma is pulled into the polar cap [Lockwood and Carlson, 1992].

At Figure 0.4d, the burst of reconnection stops and the open-closed boundary begins to relax polewards [Cowley et al., 1991]. As it moves, it pulls the blob of dense plasma within the polar cap with it, separating it from the reservoir on the dayside [Lockwood and Carlson, 1992]. Before the convection flow stops completely, Figure 0.4e, the blob of dense plasma "pinches off" from the dayside plasma to become a~~n~~ ~~independant~~ patch [Lockwood and Carlson, 1992]. The exact mechanism by which this happens is not well understood, but it is thought to be related to small variations in the IMF By component shifting the convection pattern slightly [Cowley, 1980, Lockwood and Carlson, 1992]. By Figure 0.4f, the open-closed boundary has returned completely to its original position and there is a newly formed patch ~~within~~ in the polar cap. The process can now repeat to form another patch within the polar cap.

A series of reconnection bursts can create a line of patches all propagating across the polar cap. Reconnection bursts typically last about 2 min~~utes~~ with anywhere between 7 and 25 min~~utes~~ beween bursts [Foster and Doupnik, 1984, Etemadi et al., 1988, Lockwood and Carlson, 1992]. However, observations have shown convection flow to be close to continuous for much longer periods. This can be explained by each reconnection burst exciting flow for a much longer interval than the time between bursts. In this way, a reconnection burst can excite plasma flow before the convection from the previous burst has stopped, and a series of overlapping reconnection events like this can create continuous plasma flow through the polar cap [Cowley et al., 1991].

Plasma structuring, especially at smaller scales, is often discussed in terms of the growth or damping of plasma waves, or instabilities. As discussed previously in Section 0.2.1,
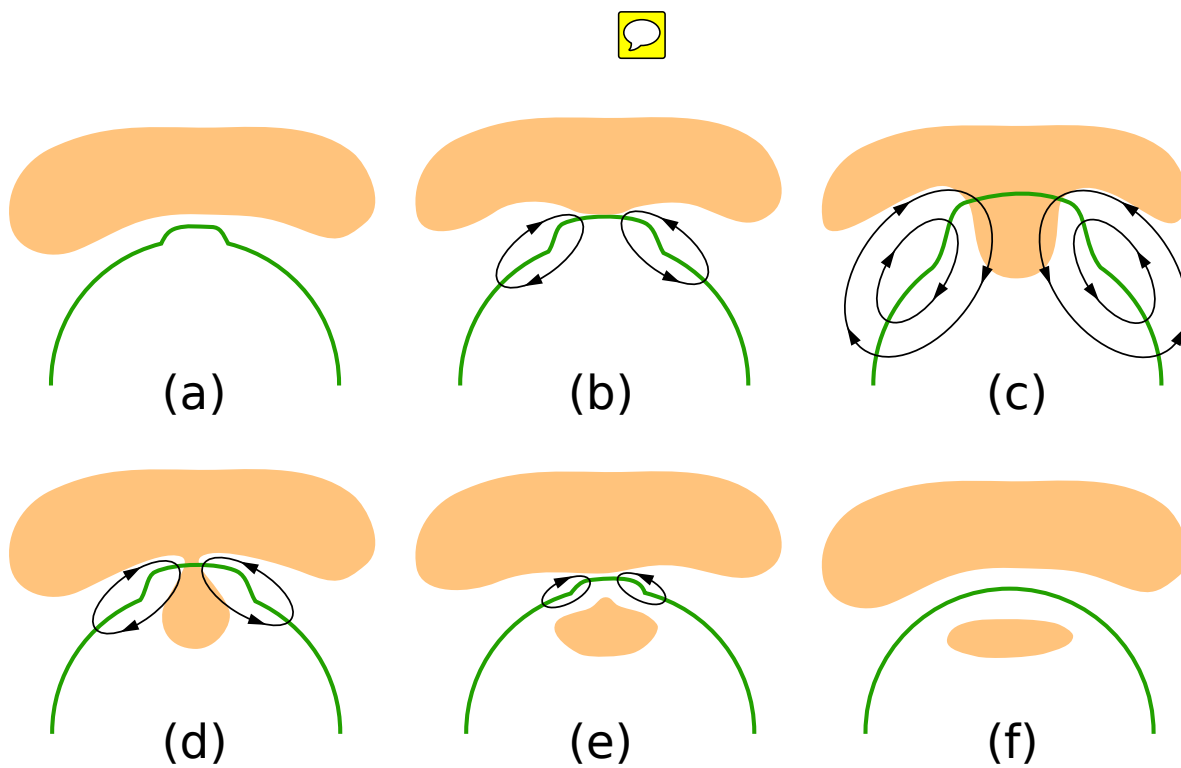
Figure 0.4. ~~Diagram of the po~~lar patch formation through transient magnetopause reconnection. The open-closed boundary is the green line. Black contours represent plasma flow. ~~Highly ionized (~~dense) daytime plasma is shown by the ~~light~~ orange regions. The burst of reconnection is occurring in Figures 0.4a–0.4c but stops in Figures 0.4d–0.4f.

the plasma characteristics change with altitude in the ionosphere, which causes a variety of different instability mechanisms to be operational depending on the region considered. The Farley-Buneman instability (FBI), or the modified two-stream instability tends to be a major factor in the E region where ion inertial effects are high [Farley, 1963, Buneman, 1963]. Also operational in the E region but more dominant at higher altitudes is the gradient-drift instability (GDI) [Simon, 1963, Hoh, 1963, Linson and Workman, 1970]. If a wave has a component along the magnetic filed line, the current-conductive instability (CCI) can be operational even if GDI is stable. Addition instabilities mechanisms emerge if shears are considered, when $\nabla E \neq 0$, such as the Kelvin-Helmholtz instability (KHI).

In the polar F-region ionosphere, GDI is typically considered the dominant structuring process [Weber et al., 1984, Cerisier et al., 1985, Basu et al., 1988, Tsunoda, 1988]. GDI is operational when high-density purturbations in the plasma move to regions of lower background density and low-density purturbations in the plasma move to regions of higher background density, such that the wave amplitude grows relative to background conditions. As plasma drifts and carries irregularities with it, the ions in high density perturbations lag behind the electrons and create a purturbed electric field. This purturbed electric field combined with the background magnetic field causes the density perturbations to $\mathbf{E} \times \mathbf{B}$ drift. If the drift causes high and low density perturbations to move as desribed above, the instability is operational and the perturbations grow. If instead high density perturbations drift into regions of higher background density and low density perturbations drift into regions of lower background density, the wave is damped.

Some of the first 1D investigations of the linear GDI growth rate found that it can be described by a simple expression involving the plasma drift velocity, $V_E = \mathbf{E} \times \mathbf{B}$, and the gradient scale length, $L = |n/(\partial n/\partial x)|$, Equation 0.4 [Simon, 1963, Hoh, 1963, Linson and Workman, 1970].

$$\gamma = \frac{V_E}{L} \tag{0.4}$$

This expression is only valid if the density gradient is in the same direction as the plasma drift velocity and the wave is propagating perpendicular to both. The results of Keskinen and Ossakow [1982, 1983], Equation 0.5, do consider an arbitrary wavevector, $\mathbf{k}$, explicitly to some extent, but still assume a general relationship between density gradients and plasma drift [Tsunoda, 1988].

$$\gamma = \frac{k_y}{k} \frac{\mathbf{k} \cdot \mathbf{V}_E}{kL} \tag{0.5}$$

The directional dependance of GDI has been shown to be significant, such that the growth rate can actually change signs (determining whether wave growth or damping occurs) with different wavevector directions, so it is important to consider this factor [Makarevich, 2014]. In addition, these expressions have historically only applicable in a particular altitudinal regieme, usually the F region.

Recently, a new expression has been introduced that considers any arbitrary wavevector, density gradient, and altitude within the ionosphere, which allows FBI, GDI, an CCI to be considered with a single dispersion relation [Makarevich, 2016].

$$(H_i - H_e)\omega = (H_i \mathbf{V}_{e0} - H_e \mathbf{V}_{i0}) \cdot \mathbf{k} + (C_i - C_e) H_e H_i \tag{0.6}$$

As before, $\mathbf{k}$ is the wavevector, ω is the wave frequency, and $\mathbf{V}_{\alpha 0}$ is the velocity of species α. The species α is given by either i for ions or e for electrons. The other quantities in equation 0.6 are not standard and described below.

$$H_\alpha = S_\alpha F_\alpha + D_\alpha^{-1} F_\parallel \qquad C_\alpha = \frac{T_\alpha}{m_\alpha \Omega_\alpha} \tag{0.7}$$

$$F_\alpha = i k_\perp^2 D_\alpha + \mathbf{G} \cdot \mathbf{k}_\perp D_\alpha + \mathbf{G} \cdot \mathbf{k} \times \hat{\mathbf{b}} \qquad F_\parallel = i k_\parallel^2 + \mathbf{G} \cdot \mathbf{k}_\parallel \tag{0.8}$$

$$S_\alpha = \frac{1}{1 + D_\alpha^2} \qquad D_\alpha = -\frac{i}{\Omega_\alpha}(\omega - \mathbf{k} \cdot V_{\alpha 0}) + r_\alpha \tag{0.9}$$

The quantity r_α is the ratio of the collision frequency to the gyrofrequency of a particular species, given by $r_\alpha = \nu_\alpha / \Omega_\alpha$.

It is useful to express Equation 0.6 in the following equivalent form by defining additional terms.

$$(D_i - D_e)\omega = \mathbf{V}_d \cdot \mathbf{k}\left(\frac{Z_2}{Z_1}\right) + (D_i \mathbf{V}_{i0} - D_e \mathbf{V}_{e0}) \cdot \mathbf{k} + (C_i - C_e) k_\perp^2 \left(\frac{Z_3}{Z_1}\right) \tag{0.10}$$

In the F region where background plasma motion is dominated by electric fields perpendicular to the magnetic field, the differential plasma velocity, $\mathbf{V}_d$, can be described as

$$\mathbf{V}_d = \mathbf{V}_{e0} - \mathbf{V}_{i0} = (r_i - r_e)\left[s_e s_i(1 + \psi)\left(R\mathbf{V}_E - \frac{\mathbf{E}}{B}\right)\right] \tag{0.11}$$

where, $s_\alpha = (1 + r_\alpha^2)^{-1}$. Additionally,

$$Z_1 = i(1 + Y) + a + Rb + ycK \qquad Z_2 = R(i + a) - b$$

$$Z_3 = -\frac{\Psi(i + a)^2}{1 + \Psi} - Rb(i + a) + \frac{b^2}{1 + \Psi} - iy(y - ic)\left[\left(K + 1 - \Psi^{-1}\right)(i + a) + Rb\left(1 - \Psi^{-1}\right)\right] \tag{0.12}$$
$$+ Ky^2(y - ic)^2$$

and

$$a = \frac{\mathbf{G} \cdot \mathbf{k}_\perp}{k_\perp^2} \qquad b = -\frac{\mathbf{G} \cdot \mathbf{k} \times \hat{\mathbf{b}}}{k_\perp^2} \qquad c = \frac{\mathbf{G} \cdot \mathbf{k}_\parallel}{k_\perp k_\parallel}$$

$$\Psi = -D_i D_e \qquad R = \frac{D_i + D_e}{1 + \Psi} \qquad y = \frac{k_\parallel}{k_\perp} \qquad K = \left(1 + \frac{1}{\Psi}\right)(1 + R^2) \qquad Y = Ky^2 \tag{0.13}$$

.

By considering certain limiting cases, an expression that is more relevant to the polar F region specifically can be resolved from Equation 0.10. First, assume a cold plasma such that the temperature of both ions and electrons is negligible. In this case, $T_\alpha = 0$, so $C_\alpha = 0$. Secondly assume all irregularities are perfectly aligned with the magnetic field such that $k_\parallel = 0$. This means that $\mathbf{k}_\perp = \mathbf{k}$, $y = 0$, and $Y = 0$. Finally, consider only low frequencies ($\omega \ll \Omega_\alpha$) and long wavelengths ($\mathbf{k} \cdot \mathbf{V}_{\alpha 0} \gg \nu_\alpha$). If D_α is expressed as shown below, it can bee seen that these limits result in the first two terms being negligible such that $D_\alpha \approx r_\alpha$.

$$D_\alpha = -i\frac{\omega}{\Omega_\alpha} + i\frac{\mathbf{k} \cdot \mathbf{V}_{\alpha 0}}{\Omega_\alpha} + \frac{\nu_\alpha}{\Omega_\alpha} \approx \frac{\nu_\alpha}{\Omega_\alpha} = r_\alpha \tag{0.14}$$

Equation 0.10 can then be expressed as follows.

$$(r_i - r_e)\omega = \mathbf{V}_d \cdot \mathbf{k}\left(\frac{Z_2}{Z_1}\right) + (r_i \mathbf{V}_{i0} - r_e \mathbf{V}_{e0}) \tag{0.15}$$

The growth rate, γ, is contained within the dispersion relation as $\omega = \omega_r + i\gamma$, so the imaginary part of Equation 0.15 must be considered separately.

$$(r_i - r_e)\gamma = \mathbf{V}_d \cdot \mathbf{k}\, \text{Im}\left\{\frac{Z_2}{Z_1}\right\} \tag{0.16}$$

The differential plasma drift has been defined previously in Equation 0.11 but the imaginary component of Z_2/Z_1 must still be identified. Using the definitions of Z_1 and Z_2 provided in Equation 0.12 and the simplifying assumptions discussed above for the F region,

$$\frac{Z_2}{Z_1} = \frac{R(i+a) - b}{i + a + Rb} \tag{0.17}$$

. Multiplying both the numerator and denominator by $-i + a + Rb$ removes the imaginary component from the denominator. Additionally the local approximation $G \ll k_\perp$ is taken, which results in a, b, and c being small so that any second order terms in these quantities can be neglected.

$$\frac{Z_2}{Z_1} = R + ib(1 + R^2) \tag{0.18}$$

Using the above result and Equation 0.11, Equation 0.16 becomes

$$(r_i - r_e)\gamma = (r_i - r_e)s_e s_i (1 + \psi) \left(R\mathbf{V}_E - \frac{E}{B} \right) \cdot \mathbf{k}b \left(1 + R^2 \right) \tag{0.19}$$

Recognizing that $s_e s_i \left(1 + R^2\right) = (1 + \psi)^{-2}$ and $b = \mathbf{G} \cdot \mathbf{k} \times \hat{\mathbf{b}}/k^2 = -\mathbf{k} \cdot \hat{\mathbf{b}} \times \mathbf{G}/k^2$ by vector identities, a final expression for the GDI growth rate in the F region can be found, which agrees well with the results of Makarevich [2014].

$$\gamma = \frac{1}{1 + \psi} \left(\hat{\mathbf{k}} \cdot \hat{\mathbf{b}} \times \mathbf{G} \right) \hat{\mathbf{k}} \cdot \left(\frac{\mathbf{E}}{B} - R\mathbf{V}_E \right) \tag{0.20}$$

In addition to analytical analysis of dispersion relations, GDI has also been studied through numerical simulations. Keskinen and Ossakow [1982] found plasma waves on the trailing edge of a large density enhancement are unstable. Keskinen and Huba [1990] expanded these results by considering coupling between the magnetosphere and ionosphere, but found that this coupling only has a substantial effect for very large-scale structuring. In addition, this simulation predicted instability evolution that was far faster than what observations had shown. 3D simulations of GDI surrounding a plasma density enhancement were introduced in Guzdar et al. [1998]. Gondarenko and Guzdar [1999] improved this 3D simulation further by including plasma dynamics parallel to the magnetic field and inertial effects. These factors are nessesary for the simulation to model secondary KHI and tertiary sheer-driven instability processes. These simulations provided insight in how exactly GDI structuring develops. Both the density and velocity spectra were found to be anisotropic, however increasing the impact of ion-inertial factors in simulations caused both spectra to become more isotropic [Gondarenko and Guzdar, 2001]. Fluctuations in density were found that were as much at 10–20% of the background plasma density [Gondarenko and Guzdar, 2004a]. Although asymmetry between structuring on the leading and trailing edges of a large-scale density structure was observed in all simulations, rapidly changing convection velocity could complicate this [Gondarenko and Guzdar, 2004b]. For instance, if a large scale structure was drifting one direction and convection patters change suddenly so that it is now drifting in the opposite direction, the leading edge becomes the trailing edge and vice versa and both edges may exhibit some structuring. Additionally, both edges may become structured if large velocity shears are initially present surrounding the density structure [Gondarenko and Guzdar, 2006]. Large shears additionally cause KHI to be operational as a primary structuring mechanism, but over time GDI will still be the dominant structuring process.

0.4.2 Observations of Polar Cap Structuring

Polar patches were first observed in the 1960s [Hill, 1963], but much of the work of characterizing them using optical and radio techniques was not accomplished until two decades later [Weber and Buchau, 1981, Weber et al., 1984, 1986, Buchau et al., 1983, 1985]. Weber and Buchau [1981] identified sun-aligned arcs that extend along the sun-earth line through large parts of the polar cap using all-sky imaging photometers (ASIP). These arcs are over 1000 km long and $\sim$ 100 km wide and are produced by soft electron precipitation. Buchau et al. [1983] used a combinations of Digisonde and ASIP measurements to identify large luminous patches in the polar cap in addition to sun-aligned arcs. These patches could have densities up to 10^6 cm^{-3} and tended to drift antisunward. Additionally, Buchau et al. [1983] found that polar patches were more likely to be observed for southward IMF B_z while sun-aligned arcs were more common for northwards B_z. Weber et al. [1984] found patches of enhanced ionization between 800–1000 km during moderately disturbed geomagnetic conditions, again using a combination of ASIP images, ionosonde measurements, and data from Dynamic Explorer 2 (DE-2). These findings confirmed that density enhancements tended to drift antisunward at speeds of 500-1000 m/s and patches were not colocated with enhanced particle precipitation within the polar cap, indicating that this is not the source of the density enhancement. Over time, the trailing edge of a patch became steeper than the leading edge and irregularities developed on the trailing edge. Conversely, Buchau et al. [1985] found that plasma densities within patches were comparable with those measured at dayside sub-auroral latitudes, suggesting that dayside solar-illuminated plasma is the source of dense plasma that form polar patches.

Coley and Heelis [1998] examined the occurrence of polar patches in both the northern and southern hemispheres with DE-2 and found that the frequency of patch occurrence was greatest when the cusp was slightly dayward of the terminator. This creates the situation of an unsunlit polar cap, so background plasma density is low and blobs of enhanced density are easily visible. In addition, the cusp then provides a gateway of highly ionized sunlit plasma into the dark polar cap. Several studies had previously reported density enhanced patches convecting from the dayside through the cusp/throat region toward the polar cap [Kelly and Vickrey, 1984, Foster and Doupnik, 1984, Foster et al., 1985, Foster, 1993]. This also agrees with observations made by Sojka and Schunk [1982], de la Beaujardière et al. [1985] Rodger and Graham [1996] also considered occurrence of patches but

with a HF radar in Halley, Antarctica. The diurnal variation in patch occurrence was found to peak at magnetic noon and the seasonal variation in equinox months. The only correlation between hourly averaged solar wind parameters that was found was a bias towards patches occurring with a negative IMF B_z component. A review of historical observations of polar patches has been provided by Crowley [1996]

The theoretical mechanism for patch formation via transient magnetic reconnection has been described previously, Section **??**. A variety of experimental evidence has been presented to support this mechanism [Cowley, 1998, Carlson and Holtet, 2002]. Experiments run in the 1980s using the European Incoherent Scatter Scientific Association (EISCAT) Tromsø, Norway ISR showed that plasma flow occurred near noon shortly after southward IMF B_z arrives at the magnetopause [Etemadi et al., 1988, Todd et al., 1988]. Later, Lockwood et al. [1993a,b] showed that these plasma flows are pulsed in the region of the polar cap boundary, as predicted by Cowley et al. [1991]. Observations made by an ASIP in Svalbard in 1984 are fully consistent with patch formation through transient magnetopause reconnection [Carlson, 1996, Carlson and Holtet, 2002]. Carlson et al. [2004] identified five signatures of transient magnetic reconnection and then examined a patch formation event for these signatures using the EISCAT Svalbard Radar. All five signatures were observed as expected, strengthening the idea that transient magnetopause reconnection is responsible for patch formation. Carlson et al. [2006] furthered this using a observations from the EISCAT Svalbard Radar, the EISCAT VHF radar in Tromsøan ASIP, and a meridian scanning photometer (MSP). They managed to identify and track a series of patches directly from the subauroral plasma reservoir and show that the boundary moves equatorward before relaxing poleward, one of the main predictions of the transient magnetopause reconnection mechanism [Lockwood and Carlson, 1992].

Recent advancements have improved the ability to image density structures in the ionosphere, particularly using multi-instrument approaches. Semeter et al. [2009] introduced a method by which the density pattern in a particular volume could be imaged in three dimensions using AMISR systems. This technique was later used by Dahlgren et al. [2012b,a] to image a polar patch. Dahlgren et al. [2012a] additionally used ASIPs and SuperDARN radars to investigate the polar patch and found that backscatter tended to be observed more on the trailing edge of the patch. This agrees well with many studies that have examined the asymmetry of small-scale plasma structuring surrounding plasma patches.

This asymmetry was first observed by Weber et al. [1984]. Backscatter power from HF radars tends to be greater on the trailing edges of both moving high-density polar structures [Milan et al., 2002] and sun-aligned arcs identified from ASIP data [Koustov et al., 2012], which is generally attributed to GDI being unstable on the trailing edge but stable on the leading edge of such large, moving density structures. Studies of patches using all-sky airglow imagers (ASI) found that the density gradient on the leading edge of polar patches tends to be 2–3 times steeper than that on the trailing edge [Hosokawa et al., 2016]. Additionally, large finger-like structures on the trailing edge of patches have been identified that were 10s–100s of kilometers in size and agree with predictions made by GDI simulations [Gondarenko and Guzdar, 2004b]. Moen et al. [2012] made direct measurements of plasma density structuring using the ICI-2 sounding rocket. This study provided evidence that decameter scale plasma structuring (the same as observed by HF radars) had spawned from kilometer scale density gradients (that observed by ASIP and ASI methods) and structuring was greatest where GDI was operational.

0.5 Motivation and Objectives

It is well accepted that the ~~polar cap ionosphere~~ is highly structured in a non-trivial manner [Carlson, 2012]. In addition to being of purely scientific interest, this structuring creates complications when sending radio waves through the ionosphere. Because the structuring is highly irregular and varies on many spatial and temporal scales, unpredictable wave refraction, phase shifts, and amplitude attenuation can occur, making signals difficult to detect. This introduces problems in any system that involves ground-to-satellite communication, such as navigation or communication. Because of the increasing interconnectedness of modern society, any interruptions or errors in these systems can have broad impacts on infrastructure, including commercial and defense interests, as well as everyday life.

The ionosphere is an important part of the highly coupled Sun-Earth environment. The polar cap ionosphere essentially serves as the boundary conditions for waves propagating through the magnetosphere. In addition, understanding plasma structuring on a range of scales is important for correctly interpreting backscatter from ionospheric radars. In particular, one of the main purposes of SuperDARN is to create large scale convection maps of both polar caps. These convection maps have been used to give context of both magnetosphere and thermosphere behavior and are widely used in space physics research. To map convection accurately, it is extremely important to understand when backscatter is

observed and when it is absent, and why this is so. Understanding plasma instability and wave growth mechanisms is very important for answering these kinds of questions. Models and simulations of structuring in the polar caps incorporate structuring mechanisms so it is helpful if these are better understood, both the operation of a particular mechanism as well as how different mechanism are interconnected and which ones may be dominant under particular conditions.

The aim of this work is to examine some of the factors (such as global solar control and GDI directional dependance) behind plasma irregularity production in the F region polar cap using both observations and theory. The majority of observational data has been found from ground based ionospheric radars, both CSR systems (Section 0.3.1) and ISR systems (Section 0.3.2), with particular emphasis on radars within the SuperDARN network, Section 0.3.1. However, these datasets have also been supplemented with information from models as well as other instruments when necessary. In addition, most experimental results are compared with predictions made by a linear fluid theory view of ionospheric plasma behavior. Specific objectives are as follows.

The first objective of is to evaluate the extent of solar control over irregularity production in the polar F region. This considers a global view of small-scale plasma structuring. The occurrence of radar backscatter will be compared with both solar illumination (considered direct solar control) and IMF factors (considered indirect solar control). This gives a macrophysical view of where and when plasma irregularities are most likely to occur.

The second objective is to investigate asymmetry in the GDI growth rate surrounding large-scale density structures. This is a modeling approach to identifying where plasma irregularities occur surrounding a polar patch and how they can be observed by a ground-based HF radar. The model allows certain factors to be considered that can be challenging to investigate experimentally because it is difficult to isolate particular effects. The model used considers the direction of a large, elongated polar patch as well as its drift direction to be arbitrary in relation to the radar and independent of each other, which gives some insight as to how structuring would be expected with polar patches in orientations that are not often observed.

The third objective is to investigate the relationship between factors that control the linear GDI growth rate and small-scale plasma structuring. This combines the theoretical consideration of where growth rate is greatest with the experimental record of where structuring is observed around a polar patch. This is particularly important because even

though plasma structuring is often observed on the trailing edge of polar patches and this is where GDI predicts the greatest growth rates, GDI theory actually predicts growth of much larger irregularities than the small scale structuring observed by HF radars. A direct comparison of the two improves our understanding of how growth rates are related to small-scale plasma structuring.

The outline of this thesis is as follows. Chapter has provided an overview of the polar ionosphere and both macro- and microphysical plasma structuring mechanisms. Chapter ?? will discuss plasma irregular occurrence and the extent to which solar factors control this occurrence. Chapter ?? will consider the directional dependance of the GDI growth rate, and in particular give recommendations for the optimal orientation between a ground-based ionospheric radar and a large-scale density structure to observe small-scale structuring. Chapter ?? will examine coincident observations made an IRS of background plasma density conditions and a CSR of small-scale plasma structuring in the polar cap and provide evidence for small-scale structuring being directionally dependent in a similar fashion to GDI predictions for large-scale plasma structuring. Chapter ?? will conclude this thesis and give a summary of the most significant results. The implications of these results will be discussed along with questions that are still open and recommendations for future research.

References

D. N. Anderson, J. Buchau, and R. A. Heelis. Origin of density enhancements in the winter polar cap ionosphere. *Radio Sci.*, 23(4):513–519, 1988.

H. Bahcivan, R. Tsunoda, M. Nicolls, and C. Heinselman. Initial ionospheric observations made by the new Resolute incoherent scatter radar and comparison to solar wind IMF. *Geophys. Res. Lett.*, 37:L15103, 2010. doi: 10.1029/2010GL043632.

L. Barthes, R. André, J.-C. Cerisier, and J.-P. Villain. Separation of multiple echoes using a high-resolution spectral analysis of SuperDARN HF radars. *Radio Sci.*, 33(4):1005–1017, 1998.

S. Basu, S. Basu, E. J. Weber, and W. R. Coley. Case study of polar cap scintillation modeling using DE 2 irregularity measurements at 800 km. *Radio Sci.*, 23(4):545–553, 1988.

D. Bilitza. Implementation of the new electron temperature model in IRI. *Adv. Space Res.*, 5(10):117–122, 1985. doi: 10.1016/0273-1177(85)90193-0.

D. Bilitza. International reference ionosphere: recent developments. *Radio Sci.*, 21:343–346, 1986. doi: 10.1029/RS021i003p00343.

D. Bilitza. International Reference Ionosphere - status 1995/1996. *Adv. Space Res.*, 20(9): 1751–1754, 1997.

D. Bilitza. International Reference Ionosphere 2000. *Radio Sci.*, 36:261–275, 2001. doi: 10.1029/2000RS002432.

D. Bilitza and K. Rawer. New options for IRI electron density in the middle ionosphere. *Adv. Space Res.*, 10(11):7–16, 1990.

D. Bilitza and B. W. Reinisch. International Reference Ionosphere 2007: Improvements and new parameters. *Adv. Space Res.*, 42(4):599–609, 2008. doi: 10.1016/j.asr.2007.07.048.

D. Bilitza, S. A. Brown, M. Y. Wang, J. R. Souza, and P. A. Roddy. Measurements and IRI model predictions during the recent solar minimum. *J. Atmos. Sol. Terr. Phys.*, 86:99–106, 2012.

D. Bilitza, D. Altadill, Y. Zhang, C. Mertens, V. Truhlik, P. Richards, L.-A. McKinnell, and B. Reinisch. The International Reference Ionosphere 2012 - a model of international collaboration. *J. Space Weather Space Clim.*, 4(A07), 2014. doi: 10.1051/swsc/201404.

K. L. Bowles. Observations of vertical-incidence scatter from the ionosphere at 41 Mc/sec. *Phys. Rev. Lett.*, 1(12):454–455, 1958.

J. Buchau, B. W. Reinisch, E. J. Weber, and J. G. Moore. Structure and dynamics of the winter polar cap F region. *Radio Sci.*, 18(6):995–1010, 1983.

J. Buchau, E. J. Weber, D. N. Anderson, H. C. Carlson, and J. G. Moore. Ionospheric structures in the polar cap: their origin and relation to 250 MHz scintillation. *Radio Sci.*, 20(3): 325–338, 1985.

O. Buneman. Excitation of field-aligned sound waves by electron streams. *Phys. Rev. Lett.*, 10:285–287, 1963.

H. C. Carlson. Incoherent scatter radar mapping of polar cap electrodynamics. *J. Atmos. Sol. Terr. Phys.*, 58:37–56, 1996.

H. C. Carlson. Sharpening our thinking about polar cap ionospheric patch morphology, research, and mitigation techniques. *Radio Sci.*, 47:RS0L21, 2012. doi: 10.1029/ 2011RS004946.

H. C. Carlson and J. A. Holtet. A voyage of discovery into the polar cap and Svalbard, 2002.

H. C. Carlson, K. Oksavik, J. Moen, and T. Pedersen. Ionospheric patch formation: Direct measurements of the origin of a polar cap patch. *Geophys. Res. Lett.*, 31:L08806, 2004. doi: 10.1029/2003GL018066.

H. C. Carlson, K. Oksavik, C. P. Nielsen, I. W. McCrea, T. R. Pedersen, and P. Gallop. Direct observations of injection events of subauroral plasma into the polar cap. *Geophys. Res. Lett.*, 33:L05103, 2006. doi: 10.1029/2005GL025230.

J. C. Cerisier, J. J. Berthelier, and C. Beghin. Unstable density gradients in the high-latitude ionosphere. *Radio Sci.*, 20(4):755–761, 1985.

G. Chisham, M. Lester, S. E. Milan, M. P. Freeman, W. A. Bristow, A. Grocott, K. A. McWilliams, J. M. Ruohoniemi, T. Yeoman, P. L. Dyson, R. A. Greenwald, T. Kikuchi, M. Pinnock, J. P. S. Rash, N. Sato, G. J. Sofko, J.-P. Villain, and A. D. M. Walker. A decade of the Super Dual Auroral Radar Network (SuperDARN): scientific achievements, new

techniques and future directions. *Surveys in Geophysics*, 28:33–109, January 2007. ISSN 0169-3298. doi: 10.1007/s10712-007-9017-8.

P. Coïsson, S. M. Radicella, R. Leitinger, and B. Nava. Topside electron density in IRI and NeQuick: Features and limitations. *Adv. Space Res.*, 37:937–942, 2006. doi: 10.1016/j.asr. 2005.09.015.

W. R. Coley and R. A. Heelis. Seasonal and universal time distribution of patches in the northern and southern polar caps. *J. Geophys. Res.*, 103(A12):29229–29237, 1998.

S. W. H. Cowley. Magnetospheric and ionospheric flow and the interplanetary magnetic field, 1980.

S. W. H. Cowley. Excitation of flow in the earth's magnetosphere-ionosphere system: observations by incoherent-scatter radar. In J. Moen, A. Egeland, and M. Lockwood, editors, *Polar Cap Boundary Phenomena*, volume 509 of *C: Mathematical and Physical Sciences*, pages 127–140. Kluwer Academic Publishers, Dordrecht, The Netherlands, 1998.

S. W. H. Cowley, M. P. Freeman, M. Lockwood, and M.F. Smith. The ionospheric signatures of flux transfer events, 1991.

G. Crowley. Critical review of ionospheric patches and blobs. In *The Review of radio science, 1993-1996*. Oxford science publications, 1996.

H. Dahlgren, G. W. Perry, J. L. Semeter, J.-P. St.-Maurice, K. Hosokawa, M. J. Nicolls, M. Greffen, K. Shiokawa, and C. Heinselman. Space-time variability of polar cap patches: Direct evidence for internal plasma structuring. *J. Geophys. Res.*, 117:A09312, sep 2012a. doi: 10.1029/2012JA017961.

H. Dahlgren, J. L. Semeter, K. Hosokawa, M. J. Nicolls, T. W. Butler, M. G. Johnsen, K. Shiokawa, and C. Heinselman. Direct three-dimensional imaging of polar ionospheric strucutes with the Resolute Bay Incoherent Scatter Radar. *Geophys. Res. Lett.*, 39:L05104, mar 2012b. doi: 10.1029/2012GL050895.

O. de la Beaujardière, V. B. Wickwar, G. Caudal, J. M. Holt, J. D. Craven, L. A. Frank, L. H. Brace, D. S. Evans, J. D. Winningham, and R. A. Heelis. Universal time dependence of nighttime F region densities at high latitudes. *J. Geophys. Res.*, 90(A5):4319–4332, 1985.

A. Etemadi, S. W. H. Cowley, M. Lockwood, B. J. I. Bromage, D. M. Willis, and H. Lühr. The dependence of high-latitude dayside ionospheric flows on the north-south component of the IMF: a high time resolution correlation analysis using EISCAT "Polar" and AMPTE UKS and IRM data. *Planet. Space Sci.*, 36(5):471–498, 1988.

J. V. Evans. Theory and practice of ionosphere study by Thomson Scatter Radar. *Proc. IEEE*, 57:496–530, 1969.

D. T. Farley. A plasma instability resulting in field-aligned irregularities in the ionosphere. *J. Geophys. Res.*, 68:6083–6093, 1963.

D. T. Farley. Multiple-pulse incoherent-scatter correlation function measurements. *Radio Sci.*, 7(6):661–666, 1972.

J. A. Fejer. Hydromagnetic wave propagation in the ionosphere. *J. Atmos. Terr. Phys.*, 18: 135–146, 1960.

J. C. Foster. Storm time plasma transport at middle and high latitudes. *J. Geophys. Res.*, 98 (A2):1675–1689, 1993.

J. C. Foster and J. R. Doupnik. Plasma convection in the vicinity of the dayside cleft. *J. Geophys. Res.*, 89(A10):9107–9113, 1984.

J. C. Foster, J. M. Holt, J. D. Kelley, and V. B. Wickwar. High-resolution observations of electric fields and F-region plasma parameters in the cleft ionosphere. In J. A. Holtet and A. Egeland, editors, *The Polar Cusp*, volume 145 of *C: Mathematical and Physical Sciences*, pages 349–364. D. Reidel Publishing Company, Dordrecht, Holland, 1985.

N. A. Gondarenko and P. N. Guzdar. Gradient drift instability in high latitude plasma patches: ion inertial effects. *Geophys. Res. Lett.*, 26(22):3345–3348, 1999.

N. A. Gondarenko and P. N. Guzdar. Three-dimensional structuring characteristics of high-latitude plasma patches. *J. Geophys. Res.*, 106(A11):24611–24620, 2001.

N. A. Gondarenko and P. N. Guzdar. Density and electric field fluctuations associated with the gradient drift instability in the high-latitude ionosphere. *Geophys. Res. Lett.*, 31: L11802, jun 2004a. doi: 10.1029/2004GL019703.

N. A. Gondarenko and P. N. Guzdar. Plasma patch structuring by the nonlinear evolution of the gradient drift instability in the high-latitude ionosphere. *J. Geophys. Res.*, 109: A09301, sep 2004b. doi: 10.1029/2004JA01054.

N. A. Gondarenko and P. N. Guzdar. Nonlinear three-dimensional simulations of mesoscale structuring by multiple drives in high-latitude plasma patches. *J. Geophys. Res.*, 111:A08302, 2006. doi: 10.1029/2006JA011701.

W. E. Gordon. Incoherent scattering of radio waves by free electrons with applications to space exploration by radar. *Proc. IEEE*, 46(11):1824–1829, 1958.

R. A. Greenwald. Space weather, SuperDARN, and the Tasmanian Tiger. *Aust. J. Phys.*, 50: 773–792, 1997.

R. A. Greenwald, W. Weiss, E. Nielsen, and N. R. Thomson. STARE: A new radar auroral backscatter in Northern Scandinavia. *Radio Sci.*, 13:1021–1029, 1978.

R. A. Greenwald, K. B. Baker, and J. P. Villain. Initial studies of small-scale F region irregularities at very high latitudes. *Radio Sci.*, 18(6):1122–1132, 1983.

R. A. Greenwald, K. B. Baker, R. A. Hutchins, and C. Hanuise. An HF phased-array radar for studying small-scale structure in the high-latitude ionosphere. *Radio Sci.*, 20(1):63–79, 1985.

P. N. Guzdar, N. A. Gondarenko, and P. K. Chaturvedi. Three-dimensional nonlinear simulations of the gradient drift instability in the high-latitude ionosphere. *Radio Sci.*, 33(6): 1901–1913, 1998.

J. Haselgrove. The hamiltonian ray path equations. *J. Atmos. Terr. Phys.*, 25:397–399, 1963.

C. J. Heinselman and M. J. Nicolls. A bayesian approach to electric field and E-region neutral wind estimation with the Poker Flat Advanced Modular Incoherent Scatter Radar. *Radio Sci.*, 43:RS5013, 2008. doi: 10.1029/2007RS003805.

G. E. Hill. Sudden enhancements of F-layer ionization in polar regions. *J. Atmos. Sci.*, 20: 492–497, 1963.

F. C. Hoh. Instability of penning-type discharges. *Phys. Fluids*, 6:1184, 1963.

K. Hosokawa, S. Taguchi, K. Shiokawa, Y. Otsuka, Y. Ogawa, and M. Nicolls. Global imaging of polar cap patches with dual airglow imagers. *Geophys. Res. Lett.*, 41, 2014. doi: 10.1002/2013GL058748.

K. Hosokawa, S. Taguchi, and Y. Ogawa. Edge of polar cap patches. *J. Geophys. Res. Space Physics*, 121:3410–3420, 2016. doi: 10.1002/2015JA021960.

R. M. Jones and J. J. Stephenson. A versatile three dimensional ray tracing computer program for radio waves in the ionosphere. Technical Report OT Report 75-76, US Dep. of Comm., Washington DC, USA, 1975.

M. C. Kelley. *The Earth's Ionosphere: Plasma Physics and Electrodynamics*. Academic Press, 2009.

J. D. Kelly and J. F. Vickrey. F-region ionospheric structure associated with antisunward flow near the dayside polar cusp. *Geophys. Res. Lett.*, 1(9):907–910, 1984.

M. J. Keskinen and J. D. Huba. Nonlinear evolution of high-latitude ionospheric interchange instabilities with scale-size-dependent magnetospheric coupling. *J. Geophys. Res.*, 95(A9):15157–15166, 1990.

M. J. Keskinen and S. L. Ossakow. Nonlinear evolution of plasma enhancements in the auroral ionosphere. I - long wavelength irregularities. *J. Geophys. Res.*, 87(A1):144–150, 1982.

M. J. Keskinen and S. L. Ossakow. Theories of high-latitude ionospheric irregularities: A review. *Radio Sci.*, 18(6):1077–1091, 1983.

A. V. Koustov, K. Hosokawa, N. Nishitani, K. Shiokawa, and H. Liu. Signatures of moving polar cap arcs in the F-region PolarDARN echoes. *Ann. Geophysicae*, 30:441–455, 2012.

L. M. Linson and J. B. Workman. Formation of striations in ionospheric plasma clouds. *J. Geophys. Res. Space Physics*, 75(16):3211–3219, 1970.

M. Lockwood and H. C. Carlson. Production of polar cap electron density patches by transient magnetopause reconnection. *Geophys. Res. Lett.*, 19(17):1731–1734, sep 1992.

M. Lockwood and S. W. H. Cowley. Ionospheric convection and the substorm cycle, jun 1992.

M. Lockwood, W. F. Denig, A. D. Farmer, V. N. Davda, S. W. H. Cowley, and H. Lühr. Ionospheric signatures of pulsed reconnection at the earth's magnetopause. *Nature*, 361: 424–428, feb 1993a.

M. Lockwood, J. Moen, S. W. H. Cowley, A. D. Farmer, U. P. Løvhaug, H. Lühr, and V. N. Davda. Variability of dayside convective and motion of the cups/cleft aurora. *Geophys. Res. Lett.*, 20(11):1011–1014, jun 1993b.

R. A. Makarevich. Symmetry considerations in the two-fluid theory of the gradient-drift instability in the lower ionosphere. *J. Geophys. Res.*, 119, 2014. doi: 10.1002/2014JA020292.

R. A. Makarevich. Towards and integrated view of ionospheric plasma instabilities: Altitudinal transitions and strong gradient case. *J. Geophys. Res. Space Physics*, 121:3634–3647, 2016. doi: 10.1002/2016JA022515.

R. A. Makarevich, L. J. Lamarche, and M. J. Nicolls. Resolute Bay Incoherent Scatter Radar observations of plasma structures in the vicinity of polar holes. *J. Geophys. Res. Space Physics*, 120, 2015. doi: 10.1002/2015JA021443.

S. E. Milan, M. Lester, and T. K. Yeoman. HF radar polar patch formation revisited: summer and winter variations in dayside plasma structuring. *Ann. Geophysicae*, 20:487–499, 2002.

G. H. Millward, R. J. Moffett, H. F. Balmforth, and A. S Rodger. Modeling the ionospheric effects of ion and electron precipitation in the cusp. *Geophys. Res. Lett.*, 104(A11):24603–24612, 1999.

J. Moen, K. Oksavik, T. Abe, M. Lester, Y. Saito, T. A. Bekkeng, and K. S. Jacobsen. First in situ measurements of hf radar echoing targets. *Geophys. Res. Lett.*, 39:L07104, 2012. doi: 10.1029/2012GL051407.

M. J. Nicolls and C. J. Heinselman. Three-dimensional measurements of traveling ionospheric disturbances with the Poker Flat Incoherent Scatter Radar. *Geophys. Res. Lett.*, 34:L21104, 2007. doi: 10.1029/2007GL031506.

M. J. Nicolls, C. J. Heinselman, E. A. Hope, S. Ranjan, M. C. Kelley, and J. D. Kelly. Imaging of polar mesosphere summer echoes with the 450 MHz Poker Flat Advanced

Modular Incoherent Scatter Radar. *Geophys. Res. Lett.*, 34:L20102, 2007. doi: 10.1029/ 2007GL031476.

E. N. Parker. Dynamics of the interplanetary gas and magnetic fields. *Astrophysical Journal*, 128:664–676, 1958.

P. V. Ponomarenko and C. L. Waters. Spectral width of SuperDARN echoes: Measurement, use and physical interpretation. *Ann. Geophysicae*, 24:115–128, 2006.

P. Prikryl, J. W. MacDougall, I. F. Grant, D. P. Steele, G. J. Sofko, and R. A. Greenwald. Observations of polar patches generated by solar wind Alfvén waves coupling to the dayside magnetosphere. *Ann. Geophysicae*, 17:463–489, 1999.

K. Rawer, S. Ramakrishnan, and D. Bilitza. Preliminary reference profiles for electron and ion densities and temperatures proposed for the International Reference Ionosphere, 1975.

K. Rawer, D. Bilitza, and S. Ramakrishnan. Goals and status of the International Reference Ionosphere. *Rev. Geophys.*, 16(2):177–181, 1978.

K. Rawer, V. Lincoln, and R. Conkright. International reference ionosphere - iri 79. Technical Report Report UAG-82, World Data Center A for Solar-Terrestrial Physics, Boulder, Colorado, USA, 1981.

H. Rishbeth and P. J. S. Williams. The EISCAT ionospheric radar: The system and its early results. *Q. J. R. Astron. Soc.*, 26:478–512, 1985.

A. S. Rodger and A. C. Graham. Diurnal and seasonal occurrence of polar patches. *Ann. Geophysicae*, 14:533–537, 1996.

A. S. Rodger, M. Pinnock, J. R. Dudeney, K. B. Baker, and R. A. Greenwald. A new mechanism for polar patch formation. *J. Geophys. Res.*, 99(A4):6425–6436, 1994.

J. M. Ruohoniemi and K. B. Baker. Large-scale imaging of high-latitude convection with Super Dual Auroral Radar Network HF radar observations. *J. Geophys. Res.*, 103:20797–20811, 1998.

J. M. Ruohoniemi, R. A. Greenwald, K. B. Baker, J.-P. Villain, and C. Hanuise. Mapping high-latitude plasma convection with coherent HF radars. *J. Geophys. Res.*, 94:13463–13477, 1989.

R. W. Schunk and A. F. Nagy. Ionospheres of the terrestrial planets. *Rev. Geophys. Space Phys.*, 18:813–852, 1980.

R. W. Schunk and A. F. Nagy. *Ionospheres: Physic, Plasma Physics, and Chemistry*. Cambridge University Press, 2 edition, 2009.

J. Semeter, T. Butler, C. Heinselman, M. Nicolls, J. Kelly, and D. Hampton. Volumetric imaging of the auroral ionosphere: Initial results from PFISR. *J. Atmos. Sol. Terr. Phys.*, 71:738–743, 2009.

A. Simon. Instability of a partially ionized plasma in a crossed electric and magnetic fields. *Phys. Fluids*, 6:382–388, 1963.

J. J. Sojka and R. W. Schunk. Predicted diurnal variations of electron density for three high-latitude incoherent scatter radars. *Geophys. Res. Lett.*, 9(2):143–146, 1982.

J. J. Sojka, M. D. Bowline, and R. W. Schunk. Patches in the polar ionosphere: UT and seasonal dependence. *J. Geophys. Res.*, 99(A8):14959–14970, 1994.

D. Themens, P. Jayachandran, M. J. Nicolls, and J. W. MacDougall. A top to bottom evaluation of IRI-2007 within the polar cap. *J. Geophys. Res.*, 119, 2014. doi: 10.1002/2014JA020052.

H. Todd, S. W. H. Cowley, A. Etemadi, B. J. I. Bromage, M. Lockwood, D. M. Willis, and H. Lühr. Flow in the high latitude ionosphere: measurements at 15 s resolution made using EISCAT "Polar" experiment. *J. Atmos. Terr. Phys.*, 50(4/5):423–446, 1988.

R. T. Tsunoda. High-latitude F region irregularities - a review and synthesis. *Geophys. Rev.*, 26:719–760, 1988.

C. E. Valladares, S. Basu, J. Buchau, and E. Friis-Christensen. Experimental evidence for the formation and entry of patches into the polar cap. *Radio Sci.*, 29(1):167–194, 1994.

C. E. Valladares, D. T. Decker, R. Sheehan, D. N. Anderson, T. Bullett, and B. W. Reinisch. Formation of polar cap patches associated with north-to-south transitions of the interplanetary magnetic field. *J. Geophys. Res.*, 103(A7):14657–14670, 1998.

E. J. Weber and J. Buchau. Polar cap F-layer auroras. *Geophys. Res. Lett.*, 8(1):125–128, 1981.

E. J. Weber, J. Buchau, J. G. Moore, J. R. Sharber, R. C. Livingston, J. D. Winningham, and B. W. Reinisch. F layer ionization patches in the polar cap. *J. Geophys. Res.*, 89(A3): 1683–1694, 1984.

E. J. Weber, R. T. Tsunoda, J. Buchau, R. E. Sheehan, D. J. Strickland, W. Whitting, and J. G. Moore. Coordinated measurements of auroral zone plasma enhancements. *J. Geophys. Res.*, 90(A7):6497–6513, 1985.

E. J. Weber, J. A. Klobuchar, J. Buchau, H. C. Carlson, R. C. Livingston, R. C. de la Beaujardiere, M. McCready, J. G. Moore, and G. J. Bishop. Polar cap F layer patches: Structure and dynamics. *J. Geophys. Res.*, 91(A11):12121–12129, 1986.